Full Length Article

# Spatial mapping of the localized corrosion behavior of a magnesium alloy AZ31B tungsten inert gas weld

Leslie G. (Bland) Miller [a,#], Corey M. Efaw [b,#], Rebecca F. Schaller [a,c], Kari Higginbotham [b], Steve D. Johns [b], Paul H. Davis [b], Elton Graugnard [b], John R. Scully [a], Michael F. Hurley [b,*]

[a] *Department of Materials Science and Engineering, University of Virginia, 395 McCormick Rd, Charlottesville, 22904-4745 VA, USA*
[b] *Micron School of Materials Science and Engineering, College of Engineering, Boise State University, 1910 University Dr, Boise, 83725-2090 ID, USA*
[c] *Materials Science and Engineering, Sandia National Laboratories, P.O. Box 5800, MS 0889, Albuquerque, 87185 NM, USA*

## Abstract

Sections of a magnesium alloy, AZ31B, joined with tungsten inert gas (TIG) welding, were examined with scanning electrochemical microscopy (SECM) and scanning Kelvin probe force microscopy (SKPFM) to investigate corrosion mechanisms by correlating observed corrosion behavior with weld-affected microstructural variations. Insight into the changing nature of the galvanic couples between weld zones and at localized microgalvanic sites were investigated using SECM and SKPFM to map both electrochemically active regions and Volta potential differences across the weld-affected zones. The formation of an Al-Zn solidification network in the fusion zone (FZ) at and near the TIG weld epicenter differs from the outer heat-affected zone (HAZ), where intermetallic particles (IMPs) are the notable secondary phase from the magnesium matrix. These microstructures were mapped with SKPFM before and after brief exposure to a salt solution, revealing micro-galvanic couples as the main driving force to corrosion initiation and propagation within each zone. The IMPs and Al-Zn solidification network act as strong cathodes and govern the corrosion processes. The galvanic coupling and evolution of the intrinsic corrosion behavior between the weld zones is explained by monitoring the hydrogen evolution reaction (HER) with SECM over time. Anodically induced cathodic activation is confirmed for this welded material, as micro-galvanic couples between microstructural features are found to transition over time to broad electrochemically active areas within the weld-affected zones, resulting in polarity reversal as time of exposure proceeds.
© 2025 Chongqing University. Publishing services provided by Elsevier B.V. on behalf of KeAi Communications Co. Ltd.
This is an open access article under the CC BY-NC-ND license (http://creativecommons.org/licenses/by-nc-nd/4.0/)
Peer review under responsibility of Chongqing University

*Keywords:* Scanning electrochemical microscopy (SECM); Scanning kelvin probe force microscopy (SKPFM); Hydrogen evolution reaction (HER); Anodically induced cathodic activation.

## 1. Introduction

Magnesium (Mg) and its alloys are excellent for the automotive and aerospace fields, given a high strength-to-weight ratio [1-3]. It is also an excellent choice in the biomedical field, as it is biocompatible and undergoes bioactivity needed for the healing process [4]. Given its low reduction potential and abundance, Mg is even an opportunistic material for rechargeable batteries, either as an active multivalent energy-transferring material [5] or within a foam framework for electrodes and current collectors [3]. Beyond applications, new methods of manufacturing soft metals like Mg (e.g., selective laser melting [6,7] or additive manufacturing [8-11]) ultimately vary the resulting micro and macrostructure, which in turn changes its degradation mechanism [12,13]. Research to understand the rapid and oftentimes unpredictable degradation rates and mechanisms of magnesium within the wide array of manufacturing practices and environments is an ongoing, complex field of investigation. In this work, the treatment of a cast and wrought magnesium alloy, AZ31B, is examined when welded, a treatment used to join structural materials that

---

* Corresponding author.
*E-mail address:* mikehurley@boisestate.edu (M.F. Hurley).
# These authors contributed equally.

reduces application density while simultaneously improving structural integrity [2,14].

Autogenous welding of Mg alloys is typically performed using either tungsten inert gas (TIG) [15-17], laser [18,19], or friction stir processes [20,21]. Regardless of the welding technique employed, the corrosion rate varies with alloy composition and microstructure, weld zone geometry, thickness, weld parameters, local environment, and immersion time in environment [19,20]. For a specific weld system, variations in the corrosion rate across the weld can be attributed to compositional and microstructural variations that develop during processing and subsequent changes in surface morphology and composition during corrosion [15,16]. Specifically, there are two main zones to consider after welding: the fusion zone (FZ) and the heat affected zones (HAZs) [15,16,22]. In the FZ, the base alloy completely melts and re-solidifies during processing, with resultant variations in the crystallographic texture, grain recrystallization/growth, and secondary phase formation during processing (e.g., element-rich solidification networking and intermetallic particles, IMPs) [15,16]. Just outside the FZ are two HAZs, which have a similar composition and texture to the wrought base, but vary in grain growth characteristics as well as IMP coalescence through Oswald ripening [23]. From the epicenter of the weld to the base metal, the transition from zone to zone is interphasial, meaning that the transition from zone to zone is not immediate and rather slowly transitions in these characteristics. Within the TIG weld of Mg-alloy AZ31B, a solidification network is rich in Al and Zn, while IMPs are typically identified as Al-Mn and Al-Mn-Fe [15,16,24]. Both the Al-Zn solidification network and IMPs function as local galvanic cathodes and sites for fast hydrogen evolution that couples to anodic Mg matrix dissolution [24]. This solidification network is densely prevalent closer to the weld epicenter, namely in the FZ, while IMPs are prominent throughout the zones impacted by welding.

To date, there has been extensive research into the mechanical behavior and failure of TIG weld joints of magnesium alloys [17,25-27]; however, little work has been published on the corrosion behavior, of which prioritizes macroscale electrochemistry and post-corrosion examination [28-30]. Previous studies by our co-authors examined corrosion of an AZ31B TIG weld in both the isolated weld zones [15] and galvanically connected weld zones [16]. Polarity reversal was observed between connected weld zones in an array of flush mounted electrodes due to variations in the cathodic kinetics over time, produced by anodically induced cathodic activation [16]. In particular, the variations in these galvanically connected weld zones were mapped on the millimeter scale utilizing multichannel multielectrode arrays (MMAs) in conjunction with *in situ* time lapse video [16]. The use of scanning probe techniques such as scanning electrochemical microscopy (SECM) and scanning Kelvin probe force microscopy (SKPFM) offers higher resolution spatial mapping and the possibility to better correlate microstructural features to localized corrosion mechanisms that drive this temporal corrosion effect.

Localized corrosion mapping techniques, such as SECM [31-34], SKPFM [35-37], scanning vibrating electrode technique (SVET) [38-42], and local electrochemical impedance spectroscopy (LEIS) [43] have all been used to probe the surface reactions on Mg alloys. In particular, SECM is valuable to examine metals and alloys that are susceptible to localized corrosion processes (e.g., micro-galvanic and pitting) by mapping on the micrometer length scale. In addition, SECM enables *in situ* measurements of electrochemical activity, a marked improvement over macroscale techniques of masking or sectioning regions to examine localized detection with MMAs [16]. SECM has been used to observe the localized corrosion events in various welds, including aluminum alloys [44], stainless steel [45], and nickel joints [46]. This includes the micro-galvanic coupling between electrochemically connected weld zones caused by slight variations in the zone's electrochemical potential after processing, driven by different area fractions of IMPs, Al-Zn solidification network, and varying compositions of the $\alpha$-Mg matrix [15,16]. The various local reactions occurring on the sample surface are specific to the anodic (e.g., $Mg \rightarrow Mg^{2+} + 2e^-$) and cathodic (e.g., $2H_2O + 2e^- \rightarrow H_2 + 2OH^-$) reactions within the material system and require accurate use of SECM techniques, including various modes, redox mediators, step sizes, scanning speeds and ultramicroelectrode (UME) sizes [47]. For SECM operated in substrate generation-tip collection (SG-TC) mode, the selection of an appropriate mediator for Mg oxidation is particularly difficult. At the substrate, since Mg oxidation is energetically favorable, it is easy to find mediators that are cathodic to the Mg anodic dissolution. However, at the UME surface, the corresponding oxidation reaction to reduce Mg ions is difficult to accomplish, as Mg has a negative reduction potential of approximately $-2.4$ V versus the standard hydrogen electrode (SHE). To address the difficulty of monitoring Mg oxidation, SECM can instead be applied to probe the rate of the hydrogen evolution (i.e., reduction) reaction (HER) that balances Mg oxidation [32]. Note that prior success has been achieved in mapping the active corrosion locations using hexaammineruthenium(III) chloride, $[Ru(NH_3)_6]Cl_3$, as a mediator that is stable over the voltage range sought to monitor HER [31].

The improved spatial resolution offered by SECM over an MMA is advantageous for mapping the development of the intrinsic weld zone corrosion rates with time, as reported elsewhere [16]. However, the fast kinetics of Mg corrosion and simultaneous hydrogen evolution [48,49] creates convective flow around the UME, thus interfering with accurate spatial detection of mediator oxidation at the UME [47]. Beyond the choice of an appropriate mediator, a less corrosive mixture of aqueous and non-aqueous electrolyte can alleviate this fast kinetic issue [50]. A semi-aqueous electrolyte, such as non-aqueous ethylene glycol mixed with an aqueous NaCl solution has been found to slow the kinetics of Mg corrosion while still enabling mapping of the active corroding sites on the Mg surface [50,51]. Similarly, the galvanic relationships in the SECM electrolyte must be considered as they can alter the cathodic and anodic characteristics of the material

observed in a chloride-enriched electrolyte. This is particularly important for Mg, which is susceptible to micro-galvanic corrosion due to sometimes small differences in the electrochemical potential between the $\alpha$-Mg matrix and secondary phases. These galvanic current differences will be important to spatially resolve the corrosion rate across the weld surface, particularly since polarity reversal has been shown to occur between AZ31B TIG weld zones in chloride environments [16].

Another scanning technique, SKPFM, is used as a surface-sensitive technique to characterize localized nanoscale variations arising from surface heterogeneities, such as IMPs [35,52]. This has been performed with some success on Mg alloys, specifically Mg-Al alloys such as AM50, AZ80 and AZ91 [36,53,54] and rare-earth containing alloys [55]. SKPFM measures the Volta potential difference between probe and sample surface, which directly relates to the relative work function [56] of various phases [57]. Though there are differences between the thermodynamic Volta potentials measured in air versus the kinetic corrosion behavior in solution, the variation in Volta potentials can indicate probable galvanic behavior when immersed into an active corrosion condition [58]. When combined with compositional information obtained from co-localized scanning electron microscopy (SEM), the observed composition-dependent Volta potential differences can then be used to predict and interpret corrosion behavior as a function of corrosive exposure. As a result, SKPFM is an important tool with nanoscale resolution to characterize the variation in microstructure and resultant corrosion properties due to the individual, intrinsic properties of various cathodic IMPs and other secondary phases in the $\alpha$-Mg matrix at a finer spatial resolution than offered even with microscale resolution typical of SECM.

In addition to well-established microgalvanic coupling behavior within Mg alloys, the process of joining similar materials to build larger parts presents new localized regions of structure, composition, and corrosion behavior. It is not clearly known how the joining process effects galvanic corrosion at the microscale and remains a critical question regarding the joining of similar alloys. In this study, SECM and co-localized SKPFM/SEM were utilized to spatially map and characterize the actively corroding regions within an AZ31B TIG weld. These techniques provide spatial resolution of electrochemical behavior associated with specific microstructural features during localized corrosion across length-scales from millimeter to sub-micron and across a temporal scale. By correlating complementary characterization techniques, the multi-scale maps of characterization data obtained were correlated with active corroding sites, taking into account characteristics of Mg welds such as microstructure, polarity reversal, and anodically induced cathodic activation [38,39,59]. A range of corrosion mechanisms were observed, wherein micro-galvanic corrosion driven by phase boundaries is observed with SKPFM, and weld zone boundaries were examined with SECM. From this work, the IMPs and the Al-Zn solidification network phases are cathodic to the $\alpha$-Mg matrix, providing a localized driving force for corrosion initiation.

Between weld zones, the FZ is initially cathodic relative to the adjacent HAZ, then there is a polarity reversal that occurs over time of exposure to a corrosive environment, where the FZ becomes the active zone relative to the HAZ. Lastly, the practice of using a mixed aqueous/non-aqueous electrolyte to slow the cathodic reaction rate of AZ31B to a point of being measurable with high-resolution *in situ* analysis is examined and discussed.

## 2. Experimental procedures

### 2.1. Materials

Commercially pure Mg (99.8 %, Alfa Aesar, Table S1) and aluminum (Al, 99.9 %, Alfa Aesar) were used to test the viability of methanol as an electrolyte component, while AZ31B (Magnesium Elektron, Table S1) was used for experimental mapping with the other techniques.

### 2.2. Weld metallurgical characterization

AZ31B was fabricated by TIG welding a sandwich structure geometry, as shown in a previous study (Fig. S1) [16]. Briefly, the top plate was drilled and countersunk at 45° to approximately 0.635 cm in diameter and welded to the bottom plate along the periphery of the countersunk hole. A Miller Syncrowave 200 TIG welder was operated at 125 Amps under Ar at 48.3 kPa with a flow rate of 18.5 L/min and air cooled without a copper chill plate. This process created large metallurgical weld zones (approximate radii progressively from the weld epicenter is 7 mm for FZ, 2 mm for HAZ1, and 9 mm for HAZ2). The HAZ regions are a transitional "interphasial" region between the FZ and unaffected wrought alloy, distinguishable by the visible secondary phase density and with elemental analysis measured on average in HAZ1 and HAZ2 (Table S1) [16]. All samples were prepared by sectioning along the welded area (Fig. S1b), followed by grinding the sectioned surface to 240 grit to remove any oxides formed prior to processing. This was followed by polishing with colloidal silica and etched with a picric acid etch made of 3 g picric acid, 30 mL acetic acid, 100 mL ethanol, and 15 mL distilled water.

Cross-sectioned samples were analyzed using an FEI Quanta 650 scanning electron microscopy (SEM). Semiquantitative compositional analysis of the IMPs, Al-Zn solidification network, FZ, HAZs and wrought material was performed using energy dispersive X-ray spectroscopy (EDS) methods with ZAF corrections, where Z is the atomic number correction, A is the absorption correction and F is the fluorescence correction, completed on the AZtec software tool [60]. Micrographs were recorded at a working distance of 10 mm while operating at an accelerating voltage of 5 kV. Compositions acquired with EDS are reported in Table S1 [16]. To aid in co-localization of SEM before and after corrosion, cross-shaped fiducial markers were inscribed on the sample surface in the bulk of the regions of interest (FZ, HAZ, and unaf-

fected bulk) using a Cascade Microtech MH2-B high resolution manual micropositioner.

### 2.3. Corrosion electrochemistry in aqueous and non-aqueous electrolytes

Prior work has shown that a mixed aqueous/non-aqueous solution can better control the cathodic kinetics to enable real-time mapping of active sites [50]. This is especially important when examining highly corrosive and active materials, such as Mg and its alloys, where the measured corrosion currents are orders of magnitude greater than other, more passive metals. Methanol is a poor solvent for sodium chloride dissolution and thus exists as a highly resistive pathway for ionic transfer. When water is incorporated, salt is more readily dissolved with existing pathways to transfer these ions. The balance of resistive and conductive electrolyte to drive kinetics at a rate which can be examined clearly with *in situ* testing methods is the basis of an aqueous and non-aqueous electrolyte formulation. Here, a better understanding of how semi-aqueous solutions affects the corrosion mechanism and rate is examined, with further refinement of the ideal solvent fractions to better resolve corrosion over time with spatial mapping techniques. In other words, the corrosion rates, as well as mechanisms were examined to find an electrolyte mixture that balances slowing of the corrosion rate with a realistic consistency of mechanism as seen in an aqueous solution. In this study, methanol (791 g/L) and deionized water (1000 g/L) were combined as co-solvents in different proportions based on weight percentages (wt.%), after which 0.1 M sodium chloride (NaCl) was added to the mixed solvent.

#### 2.3.1. Corrosion rate of Mg in mixed aqueous/non-aqueous electrolytes

Electrochemical impedance spectroscopy (EIS) was performed with a 1260A Solartron Frequency Response Analyzer between 1 mHz and 0.1 MHz to estimate corrosion rates of Mg in electrolytes of 0.1 M NaCl in a variety of water and methanol mixtures, set up in a vertical flat cell with a 1 cm$^2$ sample window. A platinum mesh was used as a counter electrode with a saturated calomel electrode (SCE, ~0.24 V vs. SHE) as a reference electrode. The equivalent circuit for a dilute solution, shown in Fig. S2, consisting of solution resistance (Rs), two resistor (R1 and R2) and capacitor (CPE1 and CPE2) couples, with an additional resistor (R3) and inductive (L) term in series made a reasonable fit over the full frequency range. The inductive loop is validated by the decreasing impedance seen at low frequencies less than 0.1 Hz. Validation of data was determined through a Kramers-Kronig (K-K) transformation, showing good correlation and low residual noise (<<1 % of calculated). From the K-K transformation, the determination of polarization resistance (R$_P$) in ohms-cm [2] is determined from the equivalent circuit [48,49,63,64].

It should be noted that this is a simplified expression that introduces some error due to the potential dependent coverage effects that can also alter the Tafel slopes, which are usually

assumed for the HER [48]. However, given the Stern-Geary equation [49,64], there is a stronger dependence of the corrosion current (i$_{corr}$) on the value of R$_P$ than the Tafel slopes, where there is a time-dependence on R$_p$ [52]. The anodic charge density consumed over time (Q), given in Coulombs per area (C/cm$^2$), can then be estimated by integrating the EIS-estimated corrosion rate over the time of exposure, with Tafel slopes estimated from literature [48]. Finally, the corrosion penetration depth (x), in cm, is determined from Faraday's second law [49]. Determination of the penetration depth as a function of corrosive environment is necessary to consider topographical evolution from corrosion, given the range limitations of the high-resolution techniques applied in this study.

The Nyquist and Bode plots, acquired from EIS after a 24-hour immersion period, for pure Mg in various 0.1 M NaCl water–methanol environments are shown in Fig. 1a-c. Two capacitive loops and an inductive loop are present in the purely aqueous spectrum [65]. However, in the environments where methanol was the dominant contributor to the electrolyte (> 50 wt.%), the inductive loop was not well defined. Equivalent circuit element values (Fig. S2) are listed in Table S2. All resistance values increased with increasing methanol, with the exception of 100 wt.% methanol (R$_p$ = 1890 ohms-cm [2]) when compared to the 99 wt.% methanol solution (R$_p$ = 2684 ohms-cm [2]). A significant increase in polarization resistance was seen when water is nearly removed from the solution, where 10 wt.% water (i.e., 90 wt.% methanol) resulted in only a polarization resistance of 555 ohms-cm [2].

The anodic charge density (Q), over the full immersion periods are listed in Table 1. In this case, the Tafel slopes ($\beta_a$ for anodic and $\beta_c$ for cathodic slopes) are approximated from King et al. [48]. The released anodic charge density decreases with increasing methanol. Similarly, corrosion rate (i$_{corr}$, observed as the inverse of polarization resistance, 1/R$_p$) decreases with increasing amounts of methanol (Fig. 1d). With the use of Faraday's second law, the penetration depth of corrosion after 24 h of immersion can be calculated for the different mixed aqueous/non-aqueous electrolytes. Replacing even a small amount of the solution with methanol can dramatically decrease the overall corrosion kinetics on pure Mg, per increase in resistance (Table S2) and penetration depth calculations (Table 1).

Pure Mg in mixed aqueous/non-aqueous (water and methanol) solutions with 0.1 M NaCl was also tested with cathodic potentiodynamic polarization scans (Fig. 1e). The cathodic kinetics were determined after 3 h at open circuit potential (OCP). Scans ranged from 0.5 mV above OCP to 2.3 V below OCP at a sweep rate of 1 mV/s. SCE was used as reference electrode. The corrosion potential has no trend with the aqueous and non-aqueous contributions to the electrolyte, all fitting within a 0.2 V range. The cathodic kinetics, wherein the HER balances magnesium oxidation/dissolution, observed here as the current density at −1.8 V versus SCE (noted with a solid line and arrow in Fig. 1e), increases with an increase in water content. In pure aqueous solution, the measured corrosion potential was −1.57 V versus SCE with cathodic kinetics
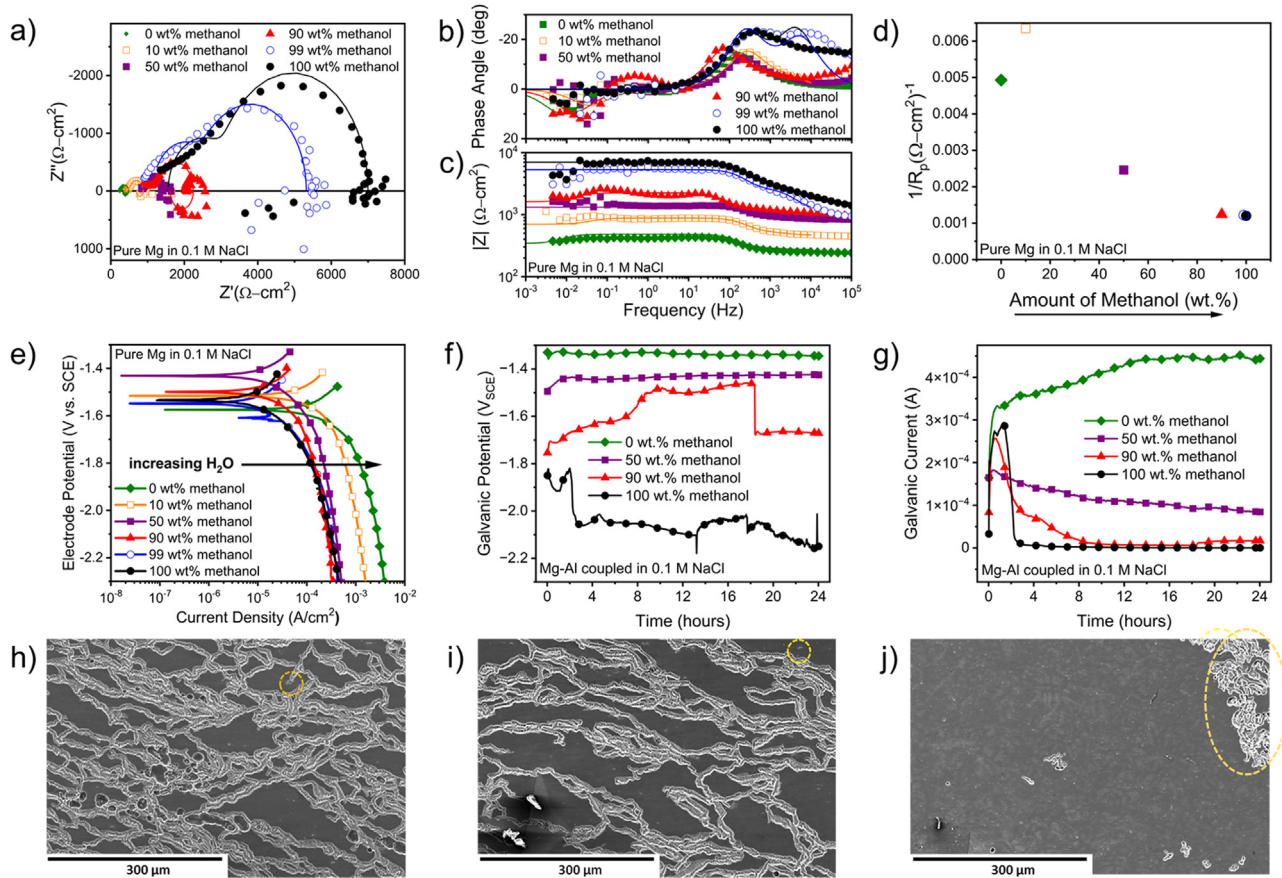
Fig. 1. Testing of various water/methanol electrolytes with 0.1 M NaCl with (a-e) pure magnesium, (f-g) magnesium coupled with aluminum, and (h-j) TIG-welded regions of AZ31B. (a) Nyquist plots, (b) Bode phase and (c) magnitude for pure magnesium in different solutions. (d) Corrosion rate of magnesium after 24 h of immersion. (e) Cathodic potentiodynamic polarization curves of pure magnesium. A line and arrow indicate where the corrosion rate is determined experimentally, increasing here with increasing water content. (f) Galvanic potential and (g) galvanic current between magnesium and aluminum. (h-j) Resultant corrosion morphology of (h) bulk AZ31B, (i) HAZ, and (j) FZ after 3 h immersion in 0.1 M NaCl in 50 wt.% water and 50 wt.% methanol. Samples were cleaned with $CrO_3$ to remove oxide films. IMPs are circled in (h-i). Filiform corrosion is circled in (j).

Table 1
Anodic charge released and corrosion penetration depth on pure magnesium calculated by integration of corrosion current density derived from electrochemical impedance spectra fitting. Tafel approximations are taken from King et al. [48].

|  | 0 wt.% methanol | 10 wt.% methanol | 50 wt.% methanol | 90 wt.% methanol | 99 wt.% methanol | 100 wt.% methanol |
|---|---|---|---|---|---|---|
| $\beta_c$ | 315.0 mV/dec | 315.0 mV/dec | 315.0 mV/dec | 315.0 mV/dec | 315.0 mV/dec | 315.0 mV/dec |
| $\beta_a$ | 112.5 mV/dec | 112.5 mV/dec | 112.5 mV/dec | 112.5 mV/dec | 112.5 mV/dec | 112.5 mV/dec |
| B | 36.0 mV/dec | 36.0 mV/dec | 36.0 mV/dec | 36.0 mV/dec | 36.0 mV/dec | 36.0 mV/dec |
| $\Sigma Q_{EIS}$ | $46.0 \pm 5$ C/cm$^2$ | $13.3 \pm 3$ C/cm$^2$ | $6.8 \pm 1.2$ C/cm$^2$ | $5.6 \pm 1.3$C/cm$^2$ | $1.2 \pm 0.5$ C/cm$^2$ | $1.6 \pm 0.3$ C/cm$^2$ |
| **x** | **33.9 μm** | **9.8 μm** | **5.0 μm** | **4.1 μm** | **0.9 μm** | **1.2 μm** |

of $\sim 1.3 \times 10^{-3}$ A/cm$^2$. Alternatively, the measured corrosion potential for the pure methanol solution was $-1.52$ V versus SCE with cathodic kinetics of $\sim 1.3 \times 10^{-4}$ A/cm$^2$, an order of magnitude less than the purely aqueous electrolyte. Again, a balance of methanol contribution to the electrolyte has a sharp "break point", wherein electrolyte with majority methanol (e.g., >50 wt.%) has a significant reduction in HER kinetics as well as reduction in corrosion current density. This was taken from the extrapolated intersection of the experimental linear "Tafel" regions observed during polarization (i.e., anodic and cathodic Tafel slopes). It was also de-

termined utilizing the Butler-Volmer relationship, yielding the corrosion current density [66].

### 2.3.2. Galvanic corrosion between Mg and Al in a mixed aqueous/non-aqueous electrolyte

The galvanic currents of coupled high purity Mg and Al planar electrodes spaced approximately 15 cm apart were determined using a zero resistance ammeter (ZRA) in a flat cell in 0.1 M NaCl aqueous solution combined with varied amounts of methanol replacing water, from 0 to 100 wt.% [61,62]. Mg was designated as the working electrode, while
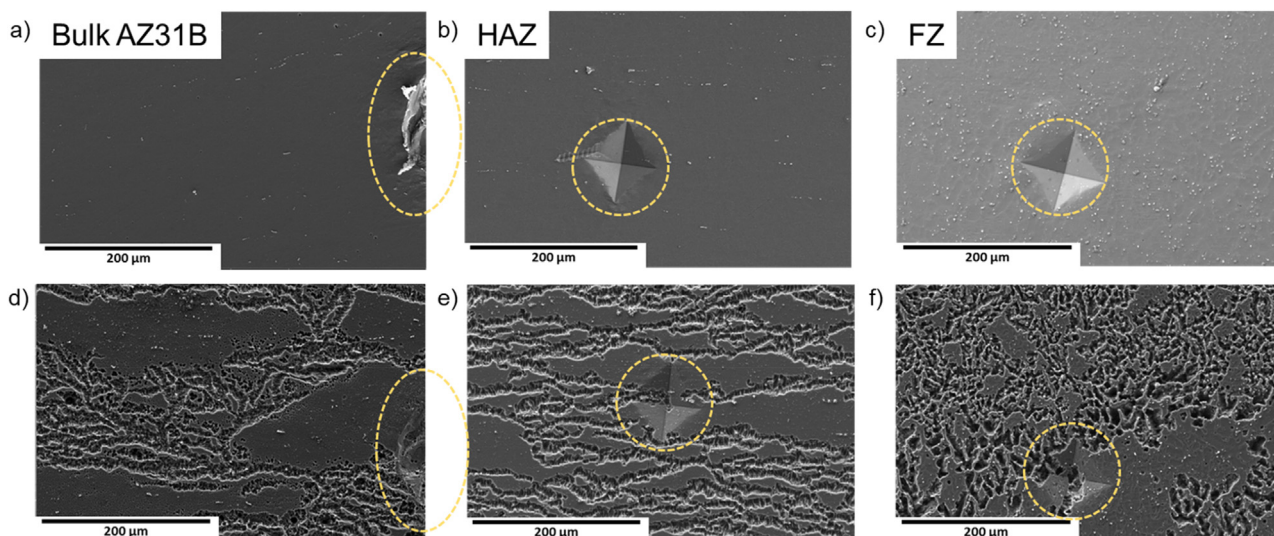
Fig. 2. (a-c) Secondary electron images of the regions of a TIG welded AZ31B: (a) bulk AZ31B, (b) HAZ, and (c) FZ. (d-f) Resultant corrosion morphology of (d) bulk AZ31B, (e) HAZ, and (f) FZ after 3 h of immersion in aqueous 0.6 M NaCl. All corroded samples were cleaned with $CrO_3$ to remove oxide films. Fiducial marks made by the micropositioner are circled in the images to help identify the same position before and after corrosion.

Al was designated as the counter electrode. The cathode to anode areal ratio was kept at 1:1 in a flat cell with a 1 cm$^2$ exposure area. All galvanic couples were tested at least three times and characteristic runs are reported herein.

At the end of 24 h in solution, both the galvanic potential (Fig. 1f) and galvanic current (Fig. 1g) between the two metals decreases with increasing methanol concentration. When methanol exceeded 50 wt.%, the galvanic potential fluctuates significantly over time, revealing instability in galvanic behavior when methanol is the dominant solvent. This is due to the poor solubility of NaCl in methanol, resulting in poor ionic conductivity. Deionized water is a good solvent to dissolve salt into ions, thus easing their mobility in solution. The right balance must be struck between an incredibly insulating, unstable electrolyte and one that degrades highly reactive Mg beyond the time and length-scales needed to examine the degradation mechanisms clearly. On one end, a highly resistive ionic pathways when methanol is the dominant solvent supports other effects such as thermal fluctuations and convection over the galvanic driving forces as the primary behavioral mechanism. On the opposite end, a purely aqueous solution drives rapid corrosion that enables convective flow around the UME and interferes with spatially resolving reaction dynamics.

### 2.3.3. . Corrosion behavior of welded regions in a mixed aqueous/non-aqueous electrolyte

The mixed aqueous/non-aqueous electrolyte of 0.1 M NaCl in 50 wt.% water and 50 wt.% methanol was examined using SEM after 3 h of exposure (Fig. 1h-j) to confirm similar overall corrosion mechanisms to the aqueous solution (Fig. 2). In the wrought base and the HAZ (Fig. 1h-i), filiform corrosion is the dominant corrosion mechanism, similar to that seen in a 0.6 M NaCl aqueous solution (Fig. 2d-e). IMPs are circled in the post-corrosion images of both the wrought base (Fig. 1h)

and the HAZ (Fig. 1i), showing some IMPs remain after corrosion initiation and propagation, corroborating past studies of these zones [15,49]. In the FZ, a greater amount of the surface remains uncorroded than in the case of 0.6 M aqueous NaCl solution (Fig. 2f), but the corroded region propagates in a similar manner along the Al-Zn network, evidenced in the circled region of Fig. 1j.

### 2.3.4. Choosing the proper mixed aqueous/non-aqueous electrolyte

For proper analysis of the *in situ* spatial mapping on Mg alloys, a balance has to be met to create a solution producing kinetics slow enough to be observed, while following the same mechanisms as an aqueous solution. This is especially true for SECM, where variations in UME-sample distance creates topography-driven artifacts (Fig. S3). On the other end, a nearly non-aqueous environment would provide an inaccurate, unrealistic depiction of the localized corrosion behavior that occurs in an aqueous, corrosive environment. In particular, when water is in moderation, the availability of the redox couple between Mg oxidation and HER is limited by thermodynamics (i.e., concentration) rather than kinetics (i.e., diffusion), thus shifting the corrosion mechanism. While a large increase in methanol content decreased the corrosion rate, it also significantly modified the electrochemical behavior. Therefore, in order to obtain a diffusion-limiting current signal at the UME used in SECM while still enabling accurate real-time mapping, a tradeoff was required. An additional consideration is in the mediator used for SECM; for instance, in this study $[Ru(NH_3)_6]Cl_3$ was used as the mediator, which is not completely soluble in methanol.

Based on these considerations, a choice of 0.1 M NaCl with 50 wt.% water and 50 wt.% methanol was found to be appropriate for the penetration depth observed and favored due to retained similarities in mechanism to the purely

aqueous electrolyte. The corrosion rate rapidly declines as methanol takes on a greater percentage of the electrolyte, slowing down the rate while maintaining the mechanism, allowing researchers to observe these mechanisms operando at a viable temporal and spatial scale. This is a useful finding for future *in situ* and operando research of highly kinetic corrosion materials, such as Mg and its alloys.

## 2.4. Scanning electrochemical microscopy

Scanning electrochemical microscopy (SECM) was performed with a VersaSCAN motion controller and VersaSTAT 3 potentiostat. A 25 µm diameter platinum UME encased in a glass insulator was used as the working electrode connected to a silver/silver chloride (Ag/AgCl, ~0.20 V vs. SHE) reference electrode. Before testing, the UME was polished using 0.25 µm polishing paste and rinsed with ethanol to ensure a clean surface. Samples were polished in ethanol up to 1 µm. Tests were initially conducted with various amounts of non-aqueous methanol added to a 0.1 M NaCl aqueous solution to slow the cathodic kinetics of the Mg-based sample. This is particularly important as the HER creates stirring of the solution at the UME, which is known to make spatial mapping of Mg by SECM difficult [67]. A solution of 50 wt.% water, 50 wt.% methanol with 0.1 M NaCl was selected [51]. Based on the ability to spatially map the HER while maintaining a steady tip current throughout the duration of the scan, 1 mM $[Ru(NH_3)_6]Cl_3$ was selected as the mediator. The reduction of $Ru(NH_3)_6^{3+}$ occurs at actively corroding sites with hydrogen oxidation reaction (HOR) as the balancing reaction, correlating the rate of evolved hydrogen reduction at the sample surface to the rate of magnesium oxidation/dissolution. At a biased UME, the mediator undergoes oxidation of $Ru(NH_3)_6^{2+}$, summarizing this methodology as the substrate-generation tip-collection (SG-TC) mode (Fig. 3a) [31,67].

The UME was positioned 30 µm above the sample surface using an approach curve, conducted at 100 µm/s. The approach curve resulted in positive feedback above the metal. The UME approached the surface until a maximum current (approximately 80 % of the steady-state signal as determined from the anodic sweep) was measured and then set at 30 µm above the surface (Fig. S4) [51]. For SECM scans, slow area scans were run at 100 µm/s with a step size of 10 µm while fast scans were run at 200 µm/s with a step size of 50 µm. Polarization voltage applied to the UME was −100 mV versus Ag/AgCl for all SECM measurements to detect HOR at the UME [31]. It should be noted that the oxygen reduction current is partially suppressed due to hindered diffusion, which makes it possible to set the UME potential at −100 mV versus Ag/AgCl to detect hydrogen evolved from the sample surface [31].

## 2.5. Scanning kelvin probe force microscopy (SKPFM)

### 2.5.1. AZ31B TIG weld surface preparation

Prior to scanning Kelvin probe force microscopy (SKPFM), the TIG welded AZ31B sample surface was me-

chanically polished at 350 rpm with successively finer grit SiC abrasive paper (LECO wet/dry 600, 800, and 1200 grit) with water lubrication. To prevent corrosion during polishing, final polishing at 400 rpm was conducted without water in a 1:3 mixture of glycerol (Fisher Chemical, Certified ACS, ≥99.5 %) to denatured ethanol (UltraPure, ACS/USP grade, 190 proof). Three grades of alumina powder (Electron Microscopy Sciences 3.0 µm $Al_2O_3$, 1.0 µm Type DX $\alpha$-$Al_2O_3$, and 0.05 µm Type DX $\gamma$-$Al_2O_3$) were individually mixed with a glycerol/ethanol lubricant to make consecutively finer slurries' and used to produce a fine finish. Residual polishing compound was removed using a clean polishing pad saturated in ethanol followed by ultrasonication in ethanol for 30 s and blow drying with compressed air. To aid in co-localization of SKPFM and SEM/EDS, cross-shaped fiducial markers were inscribed on the sample surface in the bulk of the regions of interest (FZ and HAZ) using a Cascade Microtech MH2-B high resolution manual micropositioner.

### 2.5.2. SKPFM operation

SKPFM was performed using a Bruker Dimension Icon atomic force microscope (AFM) operating with PeakForce Tapping® frequency modulation (PF FM-KPFM, Bruker). The procedure employed has been described in detail elsewhere [35,56,68]. Briefly, a PFQNE-AL probe (Bruker) acquires the sample topography using PeakForce Tapping® mode, followed by a retrace of the sample topography at a constant lift height of 100 nm above the sample surface to detect the Volta potential difference between sample and probe. All image processing and analysis were carried out using NanoScope Analysis Version 1.80. All Volta potentials reported are relative to the probe used for that data, where each probe used was calibrated versus an inert gold standard (PFKPFM-SMPL, Bruker) before and after imaging to ensure consistent results.

### 2.5.3. Post-SKPFM scanning electron microscopy (SEM)

SEM was carried out on a Hitachi S-3400 N equipped with a tungsten filament electron source. To minimize carbon deposition and resultant impact on the sample (including its corrosion behavior), secondary electron (SE) imaging was performed using an acceleration voltage of 5 kV and working distance of 10 mm. Using the fiducial markers and unique surface features present, SEM was overlaid on previously acquired SKPFM images of the same region to correlate microstructural phases with measured differences in nanoscale Volta potentials. SEM was conducted after SKPFM due to carbon deposition by the electron beam, which affects the Volta potentials measured with SKPFM [35,69].

### 2.5.4. SKPFM post-corrosion imaging

In investigations of a sample following immersion in a corrosive environment, the utility of SKPFM is limited to the early stages of corrosion filament formation. AFM tracking of high aspect ratio topography features, such as pits or corrosion filament networks, is dependent on the scan parameters and AFM tip geometry. Corrosion damage more than a few
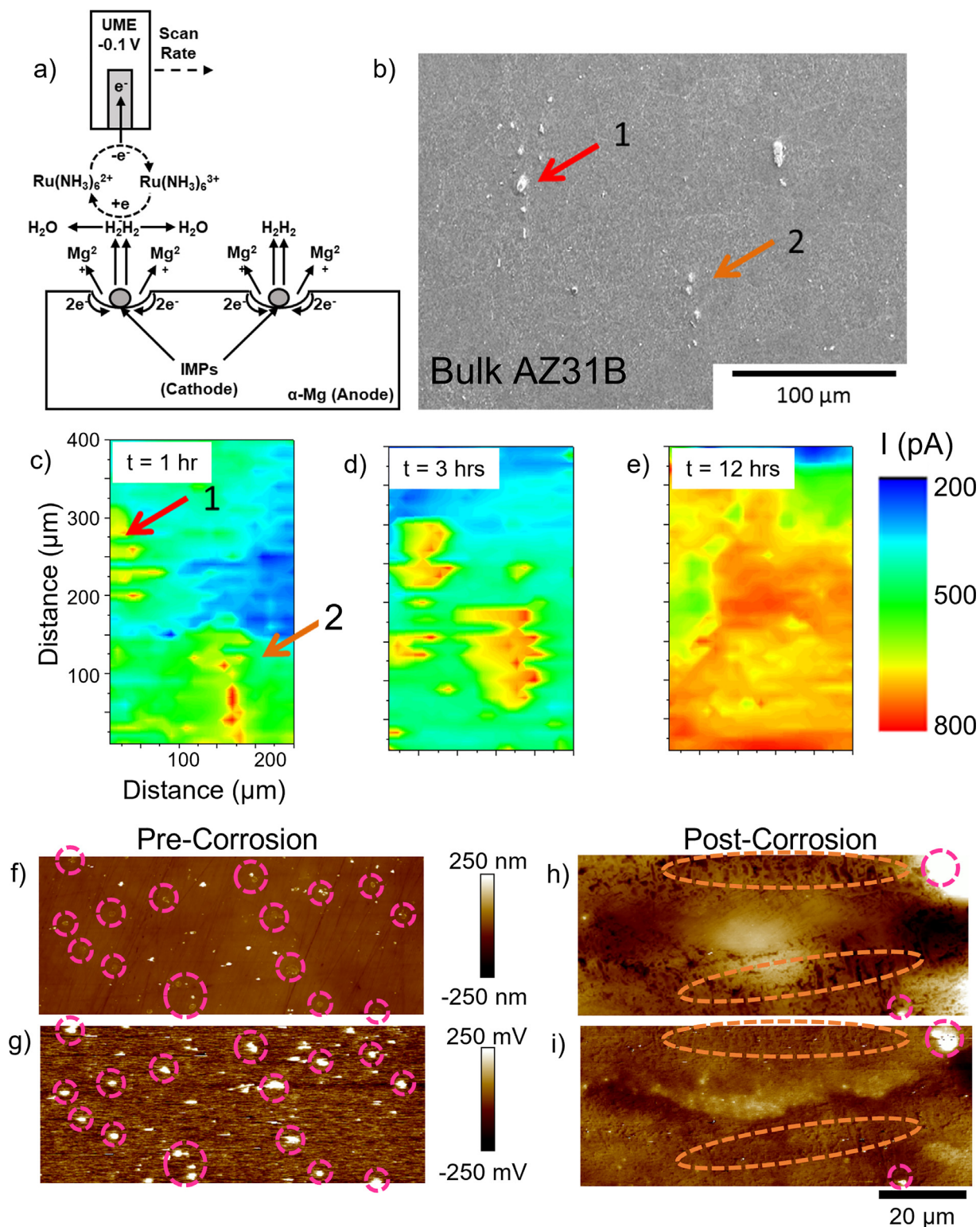
Fig. 3. Corrosion mechanism of bulk AZ31B. (a) Schematic of SECM in substrate-generation-tip-collection (SG-TC) mode with [Ru(NH$_3$)$_6$]Cl$_3$ as a mediator. During Mg corrosion, the anode half-cell reaction is Mg $\rightarrow$ Mg$^{2+}$ + 2e$^-$ with corresponding water reduction occurring by 2H$_2$O + 2e$^-$ $\rightarrow$ H$_2$ + 2OH$^-$. (b) SEM image of AZ31B, with IMPs noted at 1 and 2. (c-e) SECM scan of current on an AZ31B sample with current scale bar on the right. Time of immersion is noted in the top left corner of each SECM scan. Each image was started in the top left corner, with the fast scan in the x-direction (100 µm/s) and slow scan in the y-direction (step size of 10 µm) allowing collection of the scan in 80 s. (f) Height and (g) Volta potential images acquired with SKPFM for AZ31B, noting IMPs with pink circles. (h) Height and (i) Volta potential images acquired after exposure to 0.6 M NaCl in aqueous solution for 1 min (pink noting IMPs, orange noting filiform corrosion pathways). (For interpretation of the references to colour in this figure legend, the reader is referred to the web version of this article.)

hundred nanometers deep exceeds the threshold for accurate tracking of the sample surface with AFM. However, SKPFM characterization of the FZ after brief exposure can confirm differences in initiated local galvanic behavior. Corrosion of TIG-welded AZ31B was conducted by immersing the sample in 0.6 M aqueous NaCl solution for 1 min. The sample was then rinsed with deionized water for 5 s, rinsed with acetone for 5 s, sonicated in ethanol for 30 s, and blow dried with compressed air. The amount of corrosion damage induced via this procedure was intentionally less than in the SECM experiments due to the limited range for tracking variations in surface topography afforded by the height piezoelectric of the AFM employed for SKPFM.

## 3. Results and discussion

### 3.1. AZ31B microstructure and general corrosion behavior of welded regions

The microstructure of bulk AZ31B wrought base plate (Fig. 2a) along with the HAZs and FZ (Fig. 2b-c, respectively) of a TIG weld have been previously discussed [15,16,63]. In summary, wrought AZ31B is characterized as heavily twinned grain structure with Al-Mn and Al-Mn-Fe IMPs distributed throughout the $\alpha$-Mg matrix [15]. The composition of these IMPs are $(Fe,Mn)Al_6$ and various mixtures of binary $Al_xMn_{1-x}$, two common IMPs cited for Mg alloys containing Al and Mn (Table S1) [70]. Upon TIG welding, multiple affected zones are formed with a difference in microstructure from the wrought alloy. Two HAZs and a FZ have been identified in AZ31B TIG welds, all of which consist of a slight gradient composition to the AZ31B wrought base plate, with slightly larger Al-Mn and Al-Mn-Fe particles. Due to the high temperatures imposed during TIG welding, the FZ undergoes large grain growth in comparison to the HAZ, where twin-free grains on the order of 20 $\mu$m have been observed [15]. Al-Mn and Al-Mn-Fe IMPs are increasingly packed throughout the FZ, easily seen even with SEM here (Fig. 2c) and elsewhere [15]. Al and Zn also form a solidification network bordering the $\alpha$-Mg matrix of the FZ (Table S1) [15,16,63].

AZ31B and welded regions were examined in a highly corrosive, aqueous electrolyte (0.6 M NaCl) to validate corrosion behavior on a bulk scale, shown in Fig. 2d-f. The resultant morphology shows the AZ31B bulk material (Fig. 2d) corrodes by a filiform mechanism [71]. This morphology is similar to what is seen in the HAZ (Fig. 2e). However, a different morphology is observed in the FZ (Fig. 2f), as corrosion propagates along the Al-Zn solidification boundaries, most likely due to the galvanic coupling between the $\alpha$-Mg matrix and the Al-Zn network, confirming zone-based corrosion mechanisms in previous studies [15,16].

### 3.2. AZ31B wrought base corrosion mechanism

SECM was used on an AZ31B wrought base plate in SG-TC mode (Fig. 3a), corresponding to the SEM micrograph seen in Fig. 3b. Each SECM scan was quickly completed

($\sim$100 s) to minimize temporal drift. SECM maps were acquired starting one hour after immersion. IMPs are noted as 1 and 2 on the SEM micrograph and initial SECM map (Fig. 3b-c), revealing active hydrogen evolution initiating at these sites. After approximately 3 hours of total immersion, the region around the IMPs maintained active corrosion. However, the measured current was no longer localized to the IMP/$\alpha$-Mg interface but instead propagated and spread across the surface (Fig. 3d). Active current was widespread after prolonged exposure, seen with an SECM scan after 12 hours of immersion (Fig. 3e).

Previous SECM work on Mg alloys show that IMPs correlate to regions of large hydrogen gas flux (i.e., HER) [31]. This reaction is important for Mg corrosion, as the increase in the cathodic reaction around IMPs over time is due to the anodically induced cathodic activation phenomenon [38,59,72]. Consequently, as more of these IMPs interfacing with the $\alpha$-Mg matrix activate (i.e., the cathodic regions grow with time), the anodic region (i.e., $\alpha$-Mg matrix) coverage across the electrode diminishes [38]. Three mechanisms for this transition in galvanic areal ratio with time have been proposed: (1) Al or transition metal enrichment at the sample surface, resulting in increasing cathodic ratio as the anodic region is dissolved [24,70,73], (2) exposure of cathodic features lying immediately below the polished surface, coming to the surface as overlying anode dissolves, and (3) radial diffusion of dissolved hydrogen at IMPs [31]. In a chloride environment, the alkaline shift at these IMPs drives higher rates of $Al^{3+}$ dissolution, leading to incongruent dissolution and Al redeposition elsewhere [24,73]. Al replating can lead to increased cathodic reaction rates with time, similar to the increase in the measured HER current across the sample surface with time [38-41]. In summary, SECM reveals localized corrosion initiation at the cathode/anode interfaces as an increase in HER, propagating outward over time to progress active corrosion on the macroscale. The complex anodically induced cathodic activation phenomenon will be important to discuss when examining larger scale galvanic couples, such as the coupling between welded zones. SKPFM characterization of AZ31B following brief corrosion confirmed the activation behavior of IMPs, as the size of IMPs reduce or altogether disappear in the Volta potential channel while the topographical size of IMPs increases (circled in pink, Fig. 3f-i). Additionally, filiform corrosion tracks are visible in topography without a clear correlation to shifts in the Volta potential (circled in orange, Fig. 3h-i). Here, corrosion is initiated at the local cathode interfaces, propagating outward in a filiform mechanism, much like that seen in a bulk scale (Fig. 2d, Fig. 3c-e). Again, dissolution of IMPs and replating can occur, causing temporal changes in the corrosion driving force. Here, the brief corrosion shows how these mechanisms initiate.

### 3.3. HAZ corrosion mechanism

An SEM image of the HAZ regions into the bulk of AZ31B is shown in Fig. 4a, where IMPs become more dense
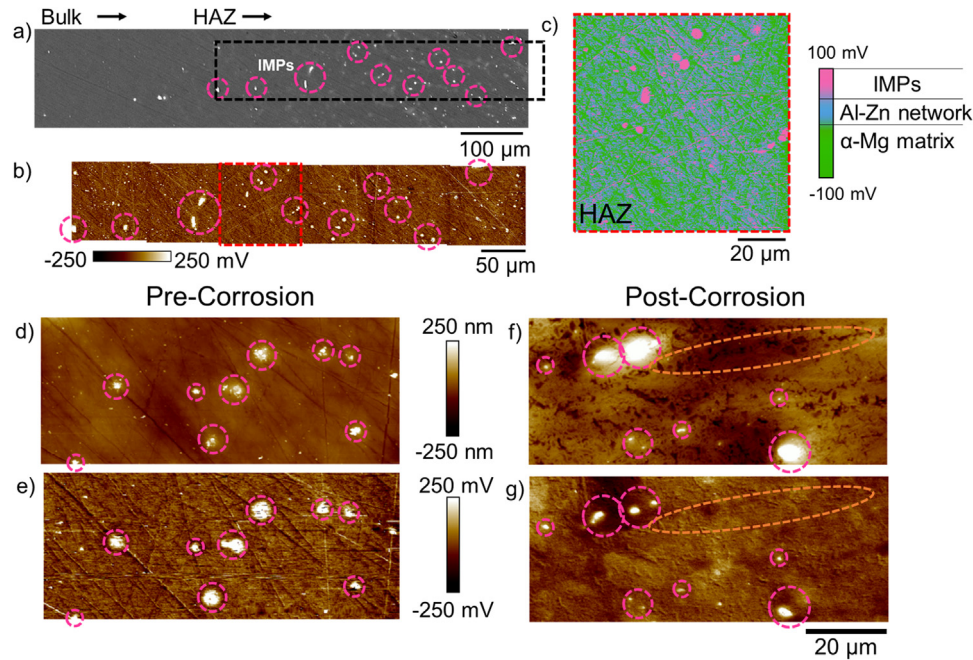
Fig. 4. Corrosion mechanism of HAZ. (a) Backscatter SEM image of HAZ, with exemplary IMPs (pink) circled and noted. (b) SKPFM montage co-localized to the black dotted box in the backscatter SEM with aligned features circled. (c) SKPFM image, from the red-outlined image of the montage in (b), with specific phases noted in the Volta potential difference scale bar. (d) Height and (e) Volta potential images acquired with SKPFM for the HAZ, noting different phases (circles note IMPs). (f) Height and (g) Volta potential difference images acquired with SKPFM for the HAZ after exposure to 0.6 M NaCl in aqueous solution for 1 min (pink noting IMPs, orange noting filiform corrosion pathway). (For interpretation of the references to colour in this figure legend, the reader is referred to the web version of this article.)

as the distance from the weld epicenter decreases. Many IMPs are noted in the SEM image that correlate to increases in the Volta potential montage acquired with SKPFM (Fig. 4b, circled in pink). In an individual SKPFM map with a more resolved scale, the Al-Zn network is not visible. Rather than resolving the Al-Zn network, the polishing direction of the HAZ reveals many of the sudden fluctuations in the Volta potential difference map (blue, Fig. 4c). This may be impacted by the surface sensitivity of the SKPFM technique; however, the prominence of the Al-Zn boundaries is lacking in the outer affected regions (i.e., HAZ and bulk AZ31B). The Volta potential for the IMPs is $\sim$260 $\pm$ 83 mV versus the $\alpha$-Mg matrix, agreeing with published data and indicative of strong local cathodes [35]. In addition, the IMPs are readily visible in high-resolution topography mapping, where the polishing rate of IMPs is significantly less than the $\alpha$-Mg matrix, resulting in their protrusion from the surface (Fig. 4d). Therefore, the prominent micro-galvanic couples visible in the HAZ is between the IMPs and $\alpha$-Mg matrix, as noted with pink circles in Fig. 4d-e. SKPFM characterization of the HAZ after brief corrosion reveals corrosion is initiated much like that seen in the bulk AZ31B (Fig. 4f-g). IMPs reduce in areas of Volta potential response when compared to the more exposed topographical areas of the cathodic sites. Filiform corrosion is also visible in the topographical data that does not strongly correlate to Volta potential differences (circled in orange).

### 3.4. Fusion zone corrosion mechanism

In Fig. 5a, a backscatter SEM image of the transition from FZ to HAZ shows a well-defined Al-Zn solidification network within the FZ that progressively dissolves into the $\alpha$-Mg matrix as the distance away from the weld epicenter increases. The black dotted rectangle indicates a co-localized region to a Volta potential montage acquired with SKPFM (Fig. 5b), showing the IMPs circled in pink with more positive Volta potentials as strong cathode sites within the weld affected zones. The number and distribution of IMPs decreases while transitioning from the FZ to the HAZ. The IMPs commonly reside within or near the Al-Zn network in the FZ (pink regions for IMPs, blue regions for the network, green for the matrix, Fig. 5c-e).

The Al-Zn network of the FZ is visible in both the backscatter image (Fig. 5a) as well as in the SKPFM results (blue regions, Fig. 5b-c). However, the boundary is clearer in the backscatter image, likely due to the greater interaction volume (i.e., greater depth) of the electron beam during SEM characterization. Since SKPFM is a surface-sensitive technique, cell walls of the connected Al-Zn boundary can only be measured where they are exposed to the surface. Regardless, the Volta potential of the Al-Zn network is lower than that of IMPs, yet higher than the $\alpha$-Mg matrix ($\sim$60 $\pm$ 31 mV vs. $\alpha$-Mg matrix). There is not necessarily a clear trend of correlating topography and Volta potential for the network, as
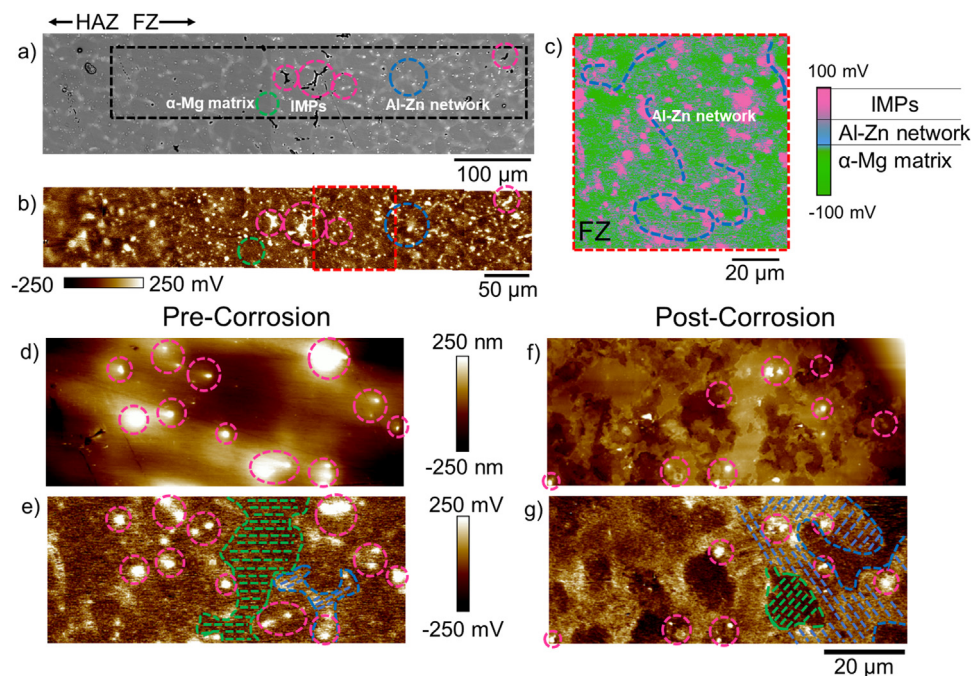
Fig. 5. Corrosion mechanism of FZ. (a) Backscatter SEM image of FZ, with exemplary IMPs (pink), Al-Zn boundaries (blue), and $\alpha$-Mg matrix (green) regions circled and noted. (b) SKPFM montage co-localized to the black dotted box in the backscatter SEM with aligned features circled. (c) SKPFM image, from the red-outlined image of the montage in (b), with specific phases noted in the Volta potential difference scale bar. Al-Zn network boundaries are noted with blue dotted lines for emphasis. (d) Height and (e) Volta potential images acquired with SKPFM for the FZ, noting different phases (circles note IMPs and selective dashed regions note network and matrix phases). (f) Height and (g) Volta potential images acquired with SKPFM for the FZ after exposure to 0.6 M NaCl in aqueous solution for 1 min, noting different phases. (For interpretation of the references to colour in this figure legend, the reader is referred to the web version of this article.)

the larger contribution of Mg to the boundary network results in a similar polishing rate as the matrix.

A post-1-minute corrosion topography (Fig. 5f) and Volta potential map (Fig. 5g) confirmed the Al-Zn boundaries as preferred cathodic sites, supporting dissolution of adjacent, anodic $\alpha$-Mg matrix. Moreover, cathodic activity was likely enhanced by the clustering of strongly cathodic IMPs within or near the Al-Zn network. IMPs appear to dissolve into solution, as there is a notable reduction in density in the Volta potential difference map and distinction in the topography map after corrosion (circled in pink), permitting probable re-plating processes. As corrosion progresses, any Al replating could also be expected to occur preferentially near cathodic regions, locally increasing the Al-Zn network surface area and height relative to the $\alpha$-Mg matrix (Fig. 5d and Fig. 5f), as well as further enhancing microgalvanic corrosion within the FZ. A possibility of this replating process is seen in Fig. 5e and Fig. 5g, where the regions of Volta potential noted as the network (blue regions) grow in size, while regions notable as $\alpha$-Mg matrix (green regions) reduce in size.

### 3.5. Zone boundary corrosion mechanism

In AZ31B TIG welds, polarity reversal has been observed at a macroscale between galvanically connected weld zones [16]. The rapid corrosion rates on the sample surface, including dissolution of IMPs in the FZ and HAZs, as well

as growth of the Al-Zn solidification network in the FZ, can lead to variations in the cathodic kinetics and OCP with time, enabling switching of which zone acts as the net galvanic anode and cathode. Over time, this polarity reversal, rather than the initial microstructure, can dominate the galvanic behavior. This phenomenon was previously captured using ZRA and MMA for electrochemically connected weld zones [16], and has now been confirmed using SECM with a rapid scan rate and large step size (Fig. 6b). Due to the large size of the weld, a fast scan rate (200 $\mu$m/s) was best suited to acquire an overall image of the actively corroding zones of a weld without the UME degrading or evolution of reactivity over time scanning (i.e., increasing current over time, Fig. S3b). However, a fast scan rate decreases the resolution of the *in situ* image and limits the ability to observe specific microstructural features less than the defined step size (50 $\mu$m in this case), such as IMPs and solidification network [15]. However, this setup can be used to see the galvanic interactions between the FZ and HAZ.

In Fig. 6a, an optical image of an AZ31B TIG weld is overlaid on an XY spatial axis in order to better visualize the approximated FZ-HAZ interphase. Corresponding SECM scans of current are shown in Fig. 6b-c over time of exposure to a 50 wt.% methanol and 50 wt.% water solution with 0.1 M NaCl and 1 mM [Ru(NH$_3$)$_6$]Cl$_3$ while under a $-100$ mV versus Ag/AgCl bias at the UME. The direction of SECM scanning did not have an effect on observable cur-
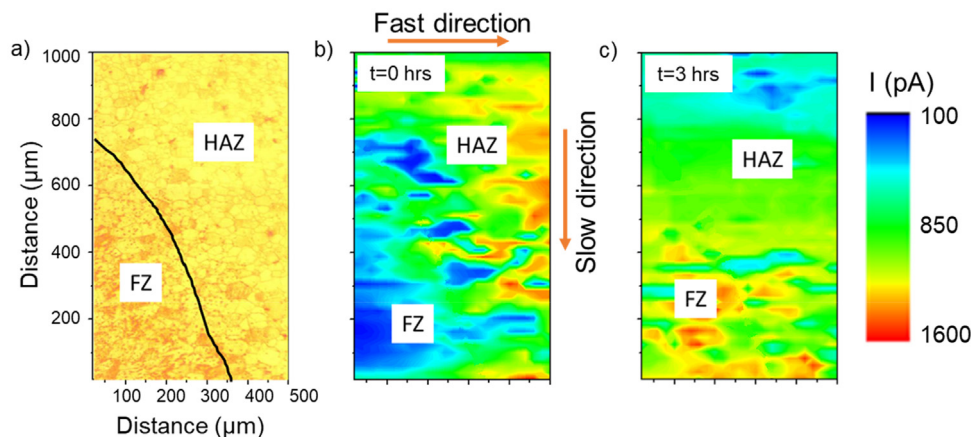
Fig. 6. SECM results of FZ and HAZ interphase of TIG weld AZ31B. (a) Optical image overlayed with general FZ and HAZ regions noted of a TIG weld AZ31B sample. (b-c) SECM scans of current on TIG weld AZ31B at 200 μm/s rate (noted with Fast direction) and 50 μm step size (noted with Slow direction) allowing collection of the scan in 50 s. FZ and HAZ regions are generally noted to correspond with the optical image. For all SECM scans, the tip is positioned 30 μm above the sample. The UME is polarized at −100 mV$_{Ag/AgCl}$. Electrolyte is 0.1 M NaCl in 50 wt.% methanol and 50 wt.% water with 1 mM [Ru(NH$_3$)$_6$]Cl$_3$ as the mediator. Time of immersion is noted in the top left corner of each SECM scan. Current ranges are displayed on the right.

rent differences, wherein scans starting in the FZ and ending in the HAZ were similar in behavior to scans starting in the HAZ and ending in the FZ. This consistency concludes that UME degradation and severe surface roughness were not factors during the fast scanning. Scanning started immediately after immersion (i.e., $t = 0$ hours), wherein the FZ is low in current relative to the HAZ (Fig. 6b), corresponding to the FZ initially corroding at a lower rate than the HAZ. The time to acquire this image is less than one minute, reiterating the reduced degradation on the UME over scanning, as well as reduced time-dependent increase in current while scanning in the slow direction. Within the FZ, corrosion initiation is primarily impacted by the boundary-matrix micro-galvanic couple (Fig. 5d-g), which has a lower relative driving force to increasing HER kinetics than the IMP-matrix micro-galvanic couple present as the main corrosion initiator in the HAZ (Fig. 4d-g). Though there are IMPs in the FZ, they do not result in as severe of a current as seen for the IMPs in the HAZ, caused by the presence of the higher area Al-Zn boundaries in the FZ.

In the second SECM scan, 3 hours after immersion, the FZ is more active than the HAZ (Fig. 6c), corresponding to the FZ now being the actively corroding weld zone. This variation in the galvanic corrosion between weld zones over time is indicative of the polarity reversal previously noted in AZ31B TIG welds [16]. Any of the three proposed mechanisms for anodically induced cathodic activation (Al enrichment, anode dissolution and cathode surface exposure, or hydrogen radial diffusion) result in a temporal shift in anode and cathode zones. In the active HAZ, continuous corrosion permits an increased cathodic presence, resulting in a polarity reversal where the FZ becomes readily active in comparison to the HAZ. This has been previously proposed and evidenced from multielectrode OCP monitoring methods. However, this work confirms the polarity reversal in real time and in galvanically coupled weld zones instead of cut slices of weld zones in a multi-electrode assembly [16].

## 4. Conclusions

- To study rapidly evolving corrosion propagation stages, methanol can be used in a mixed aqueous/non-aqueous corrosive solution to enable real-time spatial mapping of the corrosion reactions occurring for magnesium and its alloys. A mixed solution of water and methanol in equal proportions resulted in similar corrosion behavior as that seen with a concentrated salt-in-water solution, while reducing the corrosion propagation to a time-scale that is more viable to capture *in situ* of corrosion progression with SECM.

- The Al-Zn solidification network in the FZ of TIG welded AZ31B is noble relative to the surrounding Mg matrix, confirmed with SKPFM. After a short period of exposure to a corrosive environment, a microgalvanic couple between the solidification network and matrix initiates corrosion, wherein the relative cathodic network grew in size, viable in any or all of the three proposed mechanisms of Al enrichment, underlying cathode exposure, and hydrogen radial diffusion. Sustained micro-galvanic corrosion in this region changes how the FZ participates in larger scale galvanic coupling between nearby weld zones.

- IMPs in all zones of the AZ31B TIG weld (FZ, HAZ, and bulk) were seen as microgalvanic cathodes in comparison to an anodic Mg matrix as driving forces for hydrogen evolution and Mg dissolution. In the FZ, corrosion initiated at the boundaries with the matrix and enhanced the influence of the Al-Zn solidification network, as many IMPs cluster near or in the network. In the HAZ, the couple between IMPs and the matrix was the main driving force to corrosion, seen with SKPFM imaging after a short period of exposure to a corrosive environment, as well as with SECM analysis of the bulk alloy.

- SECM of the interphase between the FZ and HAZ confirmed an anodically induced cathodic activation, where aluminum was redeposited and transition metals were en-

riched in the HAZ, resulting in a time-dependent shift in galvanic coupling. The HAZ is initially active relative to the FZ, as their internal corrosion driving microgalvanic couples differ. After replating, cathodic enrichment, and/or diffusion of hydrogen in the active HAZ, a reversal in polarity occurs, where the FZ becomes the active region relative to the HAZ as cathode. This was confirmed with SECM as an operando characterization technique of the time-dependent polarity reversal.

## Conflict of interest

The authors declare that they have no known competing financial interests or personal relationships that could have appeared to influence the work reported in this paper.

## CRediT authorship contribution statement

**Leslie G. (Bland) Miller:** Writing – original draft, Investigation. **Corey M. Efaw:** Writing – original draft, Methodology, Formal analysis. **Rebecca F. Schaller:** Methodology, Investigation. **Kari Higginbotham:** Investigation. **Steve D. Johns:** Methodology, Investigation. **Paul H. Davis:** Writing – original draft, Methodology, Conceptualization. **Elton Graugnard:** Writing – review & editing, Methodology. **John R. Scully:** Writing – review & editing, Supervision, Funding acquisition. **Michael F. Hurley:** Writing – original draft, Methodology, Conceptualization.

## Acknowledgments

## Supplementary materials

Supplementary material associated with this article can be found, in the online version, at doi:10.1016/j.jma.2024.12.019.

## References

[1] S.R. Golroudbary, I. Makarava, E. Repo, A. Kraslawski, and P. Luukka: 'Magnesium Life Cycle in Automotive Industry', 29th CIRP Life Cycle Engineering Conference, 2022, Proceedia CIRP, 589-594.

[2] D.E.P. Klenam, G.S. Ogunwande, T. Omotosho, B. Ozah, N.B. Maledi, S.I. Hango, A.A. Fabuyide, L. Mohlala, J.W. van der Merwe, M.O. Bodunrin, Manuf Rev 8 (2021).

[3] H.N.G. Wadley, Adv Eng Mater 4 (10) (2002) 726–733.

[4] N. Sezer, Z. Evis, S.M. Kayhan, A. Tahmasebifar, M. Koç, J Magnes Alloy 6 (1) (2018) 23–43.

[5] H.D. Yoo, I. Shterenberg, Y. Gofer, G. Gershinsky, N. Pour, D. Aurbach, Energ Environ Sci 6 (8) (2013) 2265–2279.

[6] T. Kurzynowski, A. Pawlak, I. Smolina, Arch Civ Mech Eng 20 (1) (2020) 23.

[7] W.W. Wits, E. Amsterdam, Cirp Ann-Manuf Techn 72 (1) (2023) 129–132.

[8] R. Karunakaran, S. Ortgies, A. Tamayol, F. Bobaru, M.P. Sealy, Bioact Mater 5 (1) (2020) 44–54.

[9] J.T. Benzing, O.O. Maryon, N. Hrabe, P.H. Davis, M.F. Hurley, F.W. DelRio, Aip Adv 11 (2) (2021) 025219.

[10] M.P. Sealy, R. Karunakaran, S. Ortgies, G. Madireddy, A.P. Malshe, K.P. Rajurkar, Cirp Ann-Manuf Techn 70 (1) (2021) 179–182.

[11] Z.R. Zeng, M. Salehi, A. Kopp, S.W. Xu, M. Esmaily, N. Birbilis, J Magnes Alloy 10 (6) (2022) 1511–1541.

[12] M. Esmaily, J.E. Svensson, S. Fajardo, N. Birbilis, G.S. Frankel, S. Virtanen, R. Arrabal, S. Thomas, L.G. Johansson, Prog Mater Sci 89 (2017) 92–193.

[13] J.Y. Chen, B. Chen, Materials (Basel) (15) (2024) 17.

[14] Y.Q. Liu, D.S. Yu, Y. Zhang, J.P. Zhou, D.Q. Sun, H.M. Li, J Mater Res Technol 25 (2023) 3458–3481.

[15] L.G. Bland, J.M. Fitz-Gerald, J.R. Scully, Corrosion Journal 72 (9) (2016) 1116–1132.

[16] L.G. Bland, B.C.R. Troconis, J.S. R Jr., J.M. Fitz-Gerald, J.R. Scully, Corrosion Journal 72 (10) (2016) 1226–1242.

[17] T.T. Li, G. Song, Z.D. Zhang, L.M. Liu, Materials (Basel) 12 (13) (2019).

[18] X. Cao, M. Jahazi, J.P. Immarigeon, W. Wallace, J Mater Process Tech 171 (2) (2006) 188–204.

[19] X. Cao, M. Xiao, M. Jahazi, J. Fournier, M. Alain, Mater Manuf Process 23 (3–4) (2008) 413–418.

[20] L. Commin, M. Dumont, J.E. Masse, L. Barrallier, Acta Mater 57 (2) (2009) 326–334.

[21] J.R. Kish, G. Williams, J.R. McDermid, J.M. Thuss, C.F. Glover, J Electrochem Soc 161 (9) (2014) C405–C411.

[22] Z.P. Lu, J.H. Xu, L.H. Yu, H. Zhang, Y.Z. Jiang, J Mater Res Technol 18 (2022) 1180–1190.

[23] D.A. Porter, K.E. Easterling, Phase Transformations in Metals in Alloys, 1992, doi:10.1201/9781003011804.

[24] L.G. Bland, N. Birbilis, J.R. Scully, J Electrochem Soc 163 (14) (2016) C985-C906.

[25] H.J. Zhang, B.S. Guo, W.B. Du, X.Y. Cong, C. Chen, J Mater Res Technol 18 (2022) 3664–3672.

[26] H.F. Shi, Z.Q. Zhang, Q. Sui, X.L. Wang, X. Ren, C. Wu, W.B. Zhuang, C. Meng, Fatigue Fract Eng M 45 (11) (2022) 3167–3182.

[27] C. Meng, Z.Q. Zhang, X.L. Qiu, Y.H. Jiang, C. Wu, X.L. Wang, W.B. Zhuang, X. Ren, H.F. Shi, J Mater Res Technol 24 (2023) 7475–7496.

[28] P. Nowak, M. Mosialek, D.S. Kharitonov, J. Adamiec, A. Turowska, J Electrochem Soc (13) (2020) 167.

[29] L.M. Liu, R.Z. Xu, Corros Sci 52 (9) (2010) 3078–3085.

[30] J. Iwaszko, M. Strzelecka, Materials (Basel) (24) (2022) 15.

[31] P. Dauphin-Ducharme, R.M. Asmussen, U.M. Tefashe, M. Danaie, W.J. Binns, P. Jakupi, G.A. Botton, D.W. Shoesmith, J. Mauzeroll, J Electrochem Soc 161 (12) (2014) C557–C564.

[32] U.M. Tefashe, P. Dauphin-Ducharme, M. Danaie, Z.P. Cano, J.R. Kish, G.A. Botton, J. Mauzeroll, J Electrochem Soc 162 (10) (2015) C536–C544.

[33] D. Filotás, B.M. Fernández-Pérez, L. Nagy, G. Nagy, R.M. Souto, Sensor Actuat B-Chem (2020) 308.

[34] L.A. de Oliveira, R.M.P. da Silva, R.A. Antunes, Mater Res-Ibero-Am J 22 (5) (2019).

[35] M.F. Hurley, C.M. Efaw, P.H. Davis, J.R. Croteau, E. Graugnard, N. Birbilis, Corrosion 71 (2) (2015) 160–170.

[36] M. Jönsson, D. Thierry, N. LeBozec, Corros Sci 48 (5) (2006) 1193–1208.

[37] K. Kondoh, R. Takei, S. Kariya, S.F. Li, J. Umeda, Mater Chem Phys (2022) 279.

[38] G. Williams, N. Birbilis, H.N. McMurray, Electrochem commun 36 (0) (2013) 1–5.

[39] G. Williams, H. ap Llwyd Dafydd, R. Grace, Electrochim. Acta 109 (0) (2013) 489–501.

[40] G. Williams, H.N. McMurray, J Electrochem Soc 155 (7) (2008) C340–C349.

[41] G. Williams, K. Gusieva, N. Birbilis, Corrosion 68 (6) (2012) 489–498.

[42] R. Bolton, T. Dunlop, J. Sullivan, J. Searle, H. Heinrich, R. Westerwaal, C. Boelsma, G. Williams, J Electrochem Soc 166 (11) (2019) C3305–C3315.

[43] G. Baril, C. Blanc, M. Keddam, N. Pebere, J Electrochem Soc 150 (2003) (2010) B488–B493.

[44] A. Davoodi, Z. Esfahani, M. Sarvghad, Corros Sci 107 (2016) 133–144.

[45] K.S. de Assis, F.V.V. de Sousa, M. Miranda, I.C.P. Margarit-Mattos, V. Vivier, O.R. Mattos, Corros Sci 59 (2012) 71–80.

[46] J. Izquierdo, M.B. González-Marrero, M. Bozorg, B.M. Fernández-Pérez, H.C. Vasconcelos, J.J. Santana, R.M. Souto, Electrochim Acta 203 (2016) 366–378.

[47] S. Thomas, J. Izquierdo, N. Birbilis, R.M. Souto, Corrosion 71 (2) (2015) 171–183.

[48] A.D. King, N. Birbilis, J.R. Scully, Electrochim Acta 121 (1) (2014) 394–406.

[49] L.G. Bland, A.D. King, N. Birbilis, J.R. Scully, Corros J 71 (2 [Special Issue]) (2015) 128–145.

[50] R.M. Asmussen, W.J. Binns, P. Jakupi, P. Dauphin-Ducharme, U.M. Tefashe, J. Mauzeroll, D. Shoesmith, Corros Sci 93 (2015) 70–79.

[51] L.G. Bland, R.F. Schaller, J.R. Scully, Utilization of a Partially Non-Aqueous Electrlyte for the Spatial Mapping of Mg Corrosion Using a Model Mg-Al electrode, The Metals Society, San Diego, CA, 2016.

[52] V. Guillaumin, P. Schmutz, G.S. Frankel, J Electrochem Soc 148 (5) (2001) B163–B173.

[53] A. Pardo, M.C. Merino, A.E. Coy, F. Viejo, R. Arrabal, S. Feliú Jr, Electrochim Acta 53 (27) (2008) 7890–7902.

[54] F. Andreatta, I. Apachitei, A.A. Kodentsov, J. Dzwonczyk, J. Duszczyk, Electrochim Acta 51 (17) (2006) 3551–3557.

[55] A.E. Coy, F. Viejo, P. Skeldon, G.E. Thompson, Corros Sci 52 (12) (2010) 3896–3906.

[56] C.M. Efaw, T. da Silva, P.H. Davis, L. Li, E. Graugnard, M.F. Hurley, J Electrochem Soc 166 (11) (2019) C3018–C3027.

[57] G. Ben-Hamu, D. Eliezer, C.E. Cross, T. Böllinghaus, Mat Sci Engineer A 452–453 (2007) 210–218.

[58] P. Schmutz, G.S. Frankel, J Electrochem Soc 145 (7) (1998) 2295–2306.

[59] N. Birbilis, A.D. King, S. Thomas, G.S. Frankel, J.R. Scully, Electrochim. Acta 132 (0) (2014) 277–283.

[60] AZtecEnergy, EDS Software, Oxford Instruments, 2015 https://nano.oxinst.com/products/sem-and-fib.

[61] R. Baboian, Electrochemical Techniques for Predicting Galvanic Corrosion, in: R. Baboian, W.D. France Jr., L.C. Rowe, J.F. Rynewicz (Eds.), Galvanic and Pitting Corrosion—Field and Laboratory Studies, ASTM International, West Conshohocken, PA 19428-2959, 1976.

[62] Standard Guide for Conducting and Evaluating Galvanic Corrosion Tests in Electrolytes, *ASTM G71-G81*, 2014, ASTM International; West Conshonhocken, PA. https://www.astm.org/g0071-81r14.html.

[63] L.G. Bland, M.A. Melia, J.M. Fitz-Gerald, J.R. Scully, Corrosion 74 (7) (2018) 727–736.

[64] M. Stern, A.I. Geary, J Electrochem Soc 104 (1957) 56–63.

[65] S. Feliu, C. Maffiotte, A. Samaniego, J.C. Galvan, V. Barranco, Appl Surf Sci 257 (20) (2011) 8558–8568.

[66] D.A. Jones, 'Principles and Prevention of Corrosion', 07458, Prentice-Hall, Inc, Upper Saddle Rive, NJ, 1996.

[67] D. Polcari, P. Dauphin-Ducharme, J. Mauzeroll, Chem Rev 116 (22) (2016) 13234–13278.

[68] A. Kvryan, K. Livingston, C.M. Efaw, K. Knori, B.J. Jaques, P.H. Davis, D.P. Butt, M.F. Hurley, Metals (Basel) 6 (4) (2016) 91.

[69] C.F. Mallinson, J.F. Watts, J Electrochem Soc 163 (2016) C420–C422.

[70] R.M. Asmussen, W.J. Binns, R. Partovi-Nia, P. Jakupi, D.W. Shoesmith, Mat Corros 67 (1) (2016) 39–50.

[71] A. Samaniego, I. Llorente, S. Feliu Jr, Corros Sci 68 (2013) 66–71.

[72] G.S. Frankel, A. Samaniego, N. Birbilis, Corros Sci 70 (2013) 104–111.

[73] M. Danaie, R.M. Asmussen, P. Jakupi, D.W. Shoesmith, G.A. Botton, Corros Sci 83 (2014) 299–309.